Published in Physical Review Applied, DOI: 10.1103/PhysRevApplied.22.044071, online on 25 October 2024, Vol. 22, No. 4, 044071

Role of oxygen on structure and piezoelectric properties of $Al_{0.65}Sc_{0.35}N$ thin films

Shashidhara Acharya[1†], Xian Wang[2†], Qinwen Xu[1,3], Mingsheng Zhang[1], Jianwei Chai[1], Ping Luo[1], Poh Chong Lim[1], Ping Yang[4], Lei Shen[5], Chengliang Sun[3], Kui Yao[1*]

[1]Institute of Materials Research and Engineering (IMRE), Agency for Science, Technology and Research (A*STAR), 138634, Singapore.

[2]Chemical Engineering and Biotechnology, Nanyang Technological University, 637371, Singapore.

[3]The Institute of Technological Sciences, Wuhan University, Wuhan 430072, China.

[4]Singapore Synchrotron Light Source (SSLS), National University of Singapore, 117603, Singapore.

[5]Department of Mechanical Engineering National University of Singapore,117575, Singapore.

[*]k-yao@imre.a-star.edu.sg

[†]Authors contribute equally to this work.

Abstract

$Al_{1-x}Sc_xN$ thin films have emerged as a technologically important material for several piezoelectric and ferroelectric device applications ranging from acoustic filters, and micro-electromechanical systems (MEMS), to memories. Such applications require materials to be grown with high structural quality and optimal properties. However, it is challenging to completely eliminate oxygen contamination, which is persistently present in $Al_{1-x}Sc_xN$ thin films produced by sputtering deposition, particularly with increasing Sc content. In this study, we examine the role of oxygen on the structure and its effect on the piezoelectric and dielectric properties of $Al_{0.65}Sc_{0.35}N$ thin film. Our theoretical analysis and experimental results suggested that depending on concentration oxygen can have contrasting effects on the piezoelectric properties of $Al_{0.65}Sc_{0.35}N$ thin films. Oxygen concentration in the range of 1.2 at% to 4.3 at% severely degrades the structural coherence of the films, and consequently the piezoelectric coefficient from 10.5 to 8.2 pm/V. Electrical characterization and DFT calculations indicated the existence of defects of O_N type and ($3O_N$-V_{Al}) type depending on oxygen concentration. Our DFT calculations further suggested that at low oxygen concentrations where the substitutional defect of O_N is favored, the piezoelectric coefficient can be nearly 1.5 times higher compared to its counterpart without oxygen.

Published in Physical Review Applied, DOI: 10.1103/PhysRevApplied.22.044071, online on 25 October 2024

I. Introduction

The demonstration of fivefold enhancement in longitudinal piezoelectric coefficient (d_{33}) in scandium doped aluminum nitride ($Al_{1-x}Sc_xN$, for $x \approx 0.43$) thin films and ferroelectric switching (for $0.27 \leq x \leq 0.43$) has attracted tremendous interest for their piezoelectric and ferroelectric based device applications[1-4]. They are particularly promising for fabricating high-frequency acoustic filters, as the enhancement in d_{33} leads to an increase in the electromechanical coupling coefficient and the bandwidth of the acoustic filters[5]. For example, a bulk acoustic wave resonator based on $Al_{0.72}Sc_{0.28}N$ operating at 3 GHz with an effective electromechanical coupling coefficient (k_{eff}^2) of 16% and a figure of merit (FOM) of 158 has already been demonstrated[6]. Even a tunable frequency resonator based on $Al_{0.88}Sc_{0.12}N$ for filtering multiple bands on a single chip with an operating range of 1.96 - 2.11 GHz, k_{eff}^2 of over 10%, and FOM 87 has been developed[7]. Also, $Al_{1-x}Sc_xN$ exhibits larger remanent polarization ($P_r > 100\ \mu C/cm^2$) compared to conventional ferroelectric materials such as PZT or doped HfO_2, and ferroelectric switching has been demonstrated down to 5 nm-thick film[2,8]. In addition, $Al_{1-x}Sc_xN$ ($0 \leq x \leq 0.43$) offers several advantages over conventional piezoelectric materials such as lead zirconate titanates (PZT). Firstly, $Al_{1-x}Sc_xN$ ($x \leq 0.43$) maintains both piezoelectric and thermodynamic stability up to 1150 °C, which makes them a promising candidate for high-temperature sensor and actuator applications[9,10]. Secondly, the material possesses chemical and thermal compatibility with complementary metal-oxide-semiconductor (CMOS) backend-of-line processes. The compatibility with the fabrication techniques of microelectronic devices enables the integration of $Al_{1-x}Sc_xN$ based MEMS with CMOS technology. These features of $Al_{1-x}Sc_xN$ make it an attractive candidate for fabricating miniaturized devices through massive production with improved performance and lower cost.

The piezoelectric $Al_{1-x}Sc_xN$ ($0 \leq x \leq 0.43$) crystallizes in a wurtzite structure with polar axis along the c-axis. Beyond $x = 0.43$, $Al_{1-x}Sc_xN$ crystallizes in non-piezoelectric rock-salt structure[1,11]. Enhancement in piezoelectric coefficient (d_{33}) of wurtzite phase of $Al_{1-x}Sc_xN$ (w-$Al_{1-x}Sc_xN$) originates from elastic softening and increase in sensitivity to the strain along lattice parameter c with Sc substitution of Al[12,13]. Hence, for most of the practical applications, w-$Al_{1-x}Sc_xN$ thin films with out-of-plane orientation (002) is desirable. Several experimental works have investigated the influence of preparation conditions on the crystalline quality and orientation of the film and their correlation with piezoelectric performance. These studies indicated that the films with lower (< 2°) X-ray rocking curve full width half maximum

(FWHM) of (002) planes i.e., higher c-axis orientation had higher piezoelectric performance[11,14]. On the other hand, the exitance of misoriented grains in the films was found to degrade the film quality and thereby reduction in piezoelectric performance[14]. The formation of undesirable misoriented grains in (002) oriented w-$Al_{1-x}Sc_xN$ films is attributed to increased instability of the c-axis with increasing Sc content, underlying intermediate layer and residual stress of the film[15-17].

The presence of impurities such as oxygen in depositing atmosphere or sputtering targets was found to result in mixed polarity and affect the piezoelectric response of the films[18,19]. Due to the thermodynamically large affinity of scandium to oxygen, relatively higher oxygen contents have been found persistently in the sputtering targets and the films containing higher scandium content[20,21]. Such aliovalent impurities in w-AlN are known to create oxygen substitutional defects and compensating cation vacancy defects or [O_N - V_{Al}] defect complex[22]. Similar observations are made in w-$Al_{1-x}Sc_xN$ with oxygen impurities using photoluminescence study[23]. Further, in ferroelectric devices based on $Al_{0.7}Sc_{0.3}N$, oxygen incorporated during the deposition has been reported to induce wake-up behavior[18]. Also, a reduction in the magnitude of polarization after the wake-up behavior at temperatures above 400 °C has been observed. This would limit the high-temperature application of $Al_{1-x}Sc_xN$.

As known in general, unintentional incorporation of oxygen into $Al_{1-x}Sc_xN$ has negative impacts on final device performance. Incorporated oxygen can affect $Al_{1-x}Sc_xN$ film in multiple ways i.e., degradation of structural quality, creation of domain inversion boundary and creating charged point defects altering dielectric properties and spontaneous polarization, etc. Here we study the effect of oxygen on piezoelectric properties of $Al_{1-x}Sc_xN$ film in terms of structural coherency and point defects from both theoretical and experimental approaches. Correlating observed structural changes with electrical and piezoelectric properties revealed a reduction in structural coherency and piezoelectric coefficient with increasing oxygen concentration. From a defect point of view, DFT calculations indicated that a small concentration of oxygen substitution at the nitrogen site favors the enhancement of the piezoelectric coefficient compared to the counterpart without oxygen or with other defect complexes. Our study suggests that at higher oxygen concentrations structural coherency plays major role over the oxygen point defects on the piezoelectric properties of $Al_{1-x}Sc_xN$ film.

Published in Physical Review Applied, DOI: 10.1103/PhysRevApplied.22.044071, online on 25 October 2024

II. Methods

A. Sample preparation and characterization

$Al_{0.65}Sc_{0.35}N$ thin films were deposited on (111) TiN-coated c-sapphire substrates using a pulsed DC magnetron sputtering system. The films were deposited in an atmosphere containing Ar, N_2 and O_2 at a pressure of 7.6×10^{-4} torr. While the Ar/N_2 flow (in sccm) ratio was maintained at 2 for all the samples, the oxygen partial pressure varied from 0 to 5.6×10^{-6} torr. The depositions were carried out at ambient temperature. A pulsed DC power of 120 W of 1 μs pulse width at 10 kHz was applied on a high pure 3-inch $Al_{0.49}Sc_{0.51}$ alloy target to obtain a series of films with an approximate thickness of about 400 nm. The chemical composition of the resulting films was determined using X-ray photoelectron spectroscopy (PHI Quentera SXM Scanning X-ray microprobe), with the oxygen impurities in the range of 1.2 to 4.3 at%. The structural quality of the films was determined using a Bruker Discovery D8 X-ray diffractometer with a 2D detector and high-resolution X-ray diffractometer at Singapore synchrotron light source facility. The microstructure and morphology of the films were studied using FEI Tecnai Transmission Electron Microscope.

To determine the effective longitudinal piezoelectric coefficient ($d^*_{33,f}$) of the films, Au top electrodes with a diameter of 200 μm were deposited on the films. TiN intermediate layers were used as bottom electrodes. The $d^*_{33,f}$ values of the films were measured under alternating current (AC) using a laser scanning vibrometer (LSV, PSV OFV-3001-SF6 PolyTec GmbH)[24]. The dielectric properties of the samples were further tested using an LCR meter (HP 4294A, Agilent Technologies Inc.) under various temperatures, frequencies, and electric fields.

B. First-principles calculations

In this study, first-principles calculations were conducted using density functional theory (DFT) within the Vienna Ab-initio Simulation Package (VASP)[25,26]. The electron-core interactions were treated utilizing the projector-augmented wave (PAW) method[27], relying on plane wave basis sets. The exchange-correlation function was addressed through the generalized gradient approximation (GGA), specifically the Perdew–Burke–Ernzerhof (PBE) function[28]. Grimme's DFT-D3 method was employed to account for dispersion correction[29]. The energy cutoff was set to 600 eV. Full optimization was carried out until the force convergence on each atom was smaller than 0.01 eV/Å. The electronic iteration

convergence criterion was set to 10^{-6} eV. The Brillouin zone is sampled with a Monkhorst-Pack k-point mesh of 4×4×4 for all the calculations[30]. The piezoelectric e_{ij} tensors and Born effective charges (Z_{ij}*) are predicted by the Density Functional Perturbation Theory (DFPT) method[31,32]. The elastic constants are obtained using the energy-strain method.

C. Finite element analysis

The finite element analysis (FEA) was conducted to simulate the surface displacement response of $Al_{0.65}Sc_{0.35}N$ films using COMSOL, a commercially available tool for Multiphysics simulation. The dimensions of the experimentally fabricated device were used to construct the FEA model (see Figure S7[33]). For the simulations, the material parameters such as elastic, piezoelectric, and dielectric constants of $Al_{0.625}Sc_{0.375}N$ layers were obtained from DFT calculations and the parameters for Au, TiN, and sapphire are provided in supporting information[33]. The piezoelectric coefficient values in the FEA model were varied to fit the top surface displacement obtained by LSV measurement, which was then used to determine the actual piezoelectric coefficient (d_{33}). For the mechanical boundary conditions, the bottom of the sapphire substrate was set to a fixed boundary to assume perfect clamped conditions. For electrical boundary conditions, the bottom electrode was set to ground and an AC voltage (3 V at 10 kHz frequency) was applied to the top electrode.

III. Results

A. Structure and piezoelectric properties

A series of 400 nm-thick $Al_{0.65}Sc_{0.35}N$ films on 40 nm-thick (111) TiN on c-sapphire substrates were obtained with oxygen content varying from 1.2 at% to 4.3 at%. The chemical composition and oxygen concentration in the films were determined from the analysis of XPS core levels of each constituent element (Figure S1[33]) with an estimated uncertainty of 10 %. Prior to XPS compositional analysis, the samples were sputter cleaned for 25 mins with Ar ions with a sputter rate of 2.8 nm/min at 10 kV. We observed that after sputter cleaning the sample surface for 25 minutes, the compositional variation of the film was not significant (see supporting information Figure S2[33]). This ensures that the contribution from the surface oxide layer is avoided in determining the oxygen content of the film. The XPS analysis confirms that the oxygen concentration in the lattice of $Al_{0.65}Sc_{0.35}N$ films increases with the rise in oxygen partial pressure during the growth. 2D X-ray diffraction pattern (2D XRD) and selected area electron diffraction pattern (SAED) pattern confirm wurtzite phase $Al_{0.65}Sc_{0.35}N$ with (002) out-of-plane orientation (Figure 1). The oxygen concentration from XPS and

corresponding lattice parameters estimated from the SAED pattern are listed in Table SI (supporting information[33]). The estimated lattice parameters agree well with those reported in the literature with similar Sc concentrations[1]. The diffraction spots in Figure 1 (a, e) corresponding to $Al_{0.65}Sc_{0.35}N$ with 1.2 at% oxygen impurity, show the existence of high structural coherence in the film. As the oxygen concentration increased from 2.1 to 4.3 at%, the diffraction spot in Figure 1 (b-d) became streaky in the chi (χ) dimension. This angular spread of the diffraction spot in the 2D XRD pattern indicates an increase in mosaicity with increasing oxygen concentration. Similarly, the SAED patterns (Figure 1 f-h) of $Al_{0.65}Sc_{0.35}N$ films with oxygen concentration 2.1 to 4.3 at% show elongation of diffraction spots perpendicular to the growth direction. These results imply that increasing oxygen concentration introduces inhomogeneous structural distortion in the film thereby reducing structural coherency. The cross-sectional transmission electron micrographs of the films are presented in Figure S3 in supporting information[33]. The cross-sectional images reveal the columnar growth of the film and shows increase in misorientation of grains with increase in oxygen content.

Further, we investigated the XRD peak broadening in the omega (ω) dimension using an X-ray rocking curve at the position of $Al_{0.65}Sc_{0.35}N$ (002) Bragg reflection (Figure 2a). The FWHM of the rocking curves is determined by fitting a pseudo-Voight function. As seen from Figure 2b, the FWHM increased from $2.4 \pm 0.02°$ to $7.9 \pm 0.12°$ with increasing oxygen concentration from 1.2 at% to 4.3 at%. The broadening of the peak could be due to several reasons such as the reduction of coherently scattering domain, accumulation of defects or dislocations, and local lattice strain. The peak fitting of rocking curves suggested that peaks are Gaussian in shape. Broadening of the rocking curve with a Gaussian peak shape is commonly ascribed to imperfections and misorientations of a set of planes[34,35]. The peak width of the (002) rocking curve in our scenario is therefore mostly caused by the increased misorientation of the (002) plane with respect to surface normal.

Published in Physical Review Applied, DOI: 10.1103/PhysRevApplied.22.044071, online on 25 October 2024

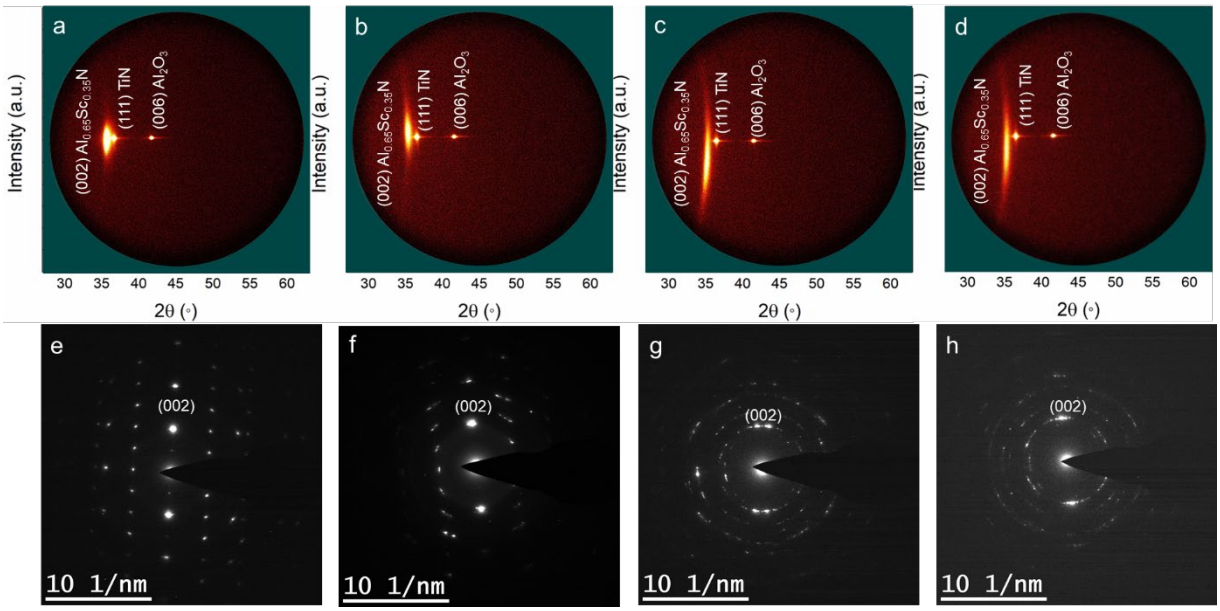

Figure 1. Structural analysis of $Al_{0.65}Sc_{0.35}N$ films using XRD (a-d) and TEM (e-h) with oxygen content of (a, e) 1.2 at%, (b, f) 2.1 at%, (c, g) 2.6 at % and (d, h) 4.3 at%.

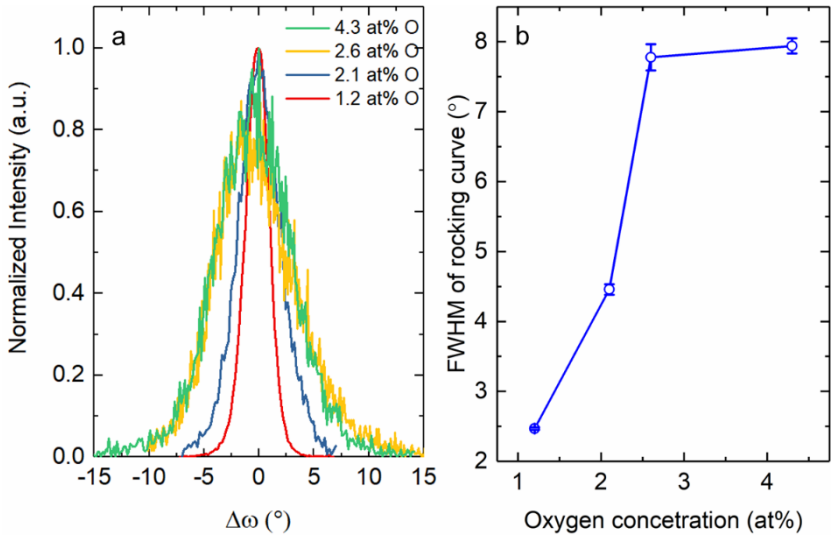

Figure 2. Misorientation of grains in $Al_{0.65}Sc_{0.35}N$. (a) Omega (ω) scan of (002) peak of $Al_{0.65}Sc_{0.35}N$ films with oxygen content 1.2 at% to 4.3 at%. (b) FWHM of (002) peaks of $Al_{0.65}Sc_{0.35}N$ films as a function of oxygen content.

The lattice parameter of $Al_{0.65}Sc_{0.35}N$ films remains almost constant with increasing oxygen content from 1.2 at% to 4.3 at% and the observed variations in experimental data are within the estimation error. Previous studies on oxygen incorporation in wurtzite AlN suggest that oxygen has limited solubility in AlN, and the amount of incorporation depends on the growth method. In the case of single crystal growth, which involves high temperature and

equilibrium conditions, oxygen incorporation is around 0.75%[36]. Whereas in low-temperature growth conditions such as sputter depositions oxygen incorporation in grains can be up to 8%[37]. Further addition of oxygen is found to form amorphous grain boundary phase that increases in volume with increasing oxygen content. Based on this, we can conclude that in our case only a fraction of oxygen may be incorporated into the lattice and the rest of the oxygen at the grain boundary region.

To study the piezoelectric response of $Al_{0.65}Sc_{0.35}N$ films with oxygen impurities we measured the displacement of the film surface using a laser scanning vibrometer (LSV) under an AC electric field at 10 kHz. The displacement signals were obtained from multiple points by scanning across a larger area that includes the top electrode and its surrounding film area (see Figure S4[33]). Covering a large area allows for easy correction of errors caused by substrate bending or movement, which is difficult with several single-point measurement techniques. The effective longitudinal piezoelectric coefficient ($d^*_{33,f}$) is then calculated from the net surface displacement. Figure 3a shows the dependence of the $d^*_{33,f}$ of $Al_{0.65}Sc_{0.35}N$ films on oxygen impurity concentration. As oxygen concentration increased, the piezoelectric response of $Al_{0.65}Sc_{0.35}N$ films was found to degrade with $d^*_{33,f}$ decreasing from 7.1 ± 0.04 pm/V (1.2 at% oxygen) to 5.5 ± 0.09 pm/V (for 4.3 at% oxygen). The $d^*_{33,f}$ value for $Al_{0.65}Sc_{0.35}N$ film even with low oxygen (1.2 at%) and coherent structure (square symbols in Figure 3a) is considerably lower than those reported for a similar composition[1,38]. However, the comparison of piezoelectric coefficients measured using different methods is not straightforward, as the measured values depend on electrode size and mechanical boundary conditions. For instance, the values determined by the Berlincourt method and single-beam interferometer are reported to be affected by the electrode size and substrate bending effect[39,40]. In our case, the substrate bending effect is minimized by using an optimal top electrode size and fixing the back side of the substrate to a rigid holder. Also, when an electric field is applied to a piezoelectric film, displacement can occur on both surface and interface (film/substrate)[41,42]. Since the interface is constrained by the substrate, the extent of displacement at the interface is unknown. As a result of this the measured value of $d^*_{33,f}$ can be substantially lower than the actual d_{33}.

To determine the actual piezoelectric coefficient, we applied finite element analysis (FEA) to simulate the complete displacement profile of the film including top and bottom surface deformation at the active region. In the simulation, we varied the piezoelectric

coefficient of the films to fit the experimental data of top surface displacement (see Table I). Figure 3a (circle symbols) shows the piezoelectric coefficient (d_{33}) obtained by FEA simulations and fitting approach for $Al_{0.65}Sc_{0.35}N$ films with different oxygen content. Figure 3b shows the corresponding displacement profile of the top and bottom surfaces of the films. It is evident from the simulation results that there is considerable deformation at the interface between the film and substrate. Hence, it becomes essential to use displacement measurement and subsequent FEA simulation to determine a more precise real piezoelectric coefficient in the case of films elastically constrained by the substrate. Table I presents the piezoelectric coefficients obtained by LSV measurement, FEA simulations and DFT calculations. The difference in the piezoelectric coefficients determined by the combined approach of measurement and FEA simulation compared to the DFT calculated could be due to several reasons such as DFT calculation does not account for substrate constraint and increased mosaicity caused by oxygen in $Al_{0.65}Sc_{0.35}N$ films.

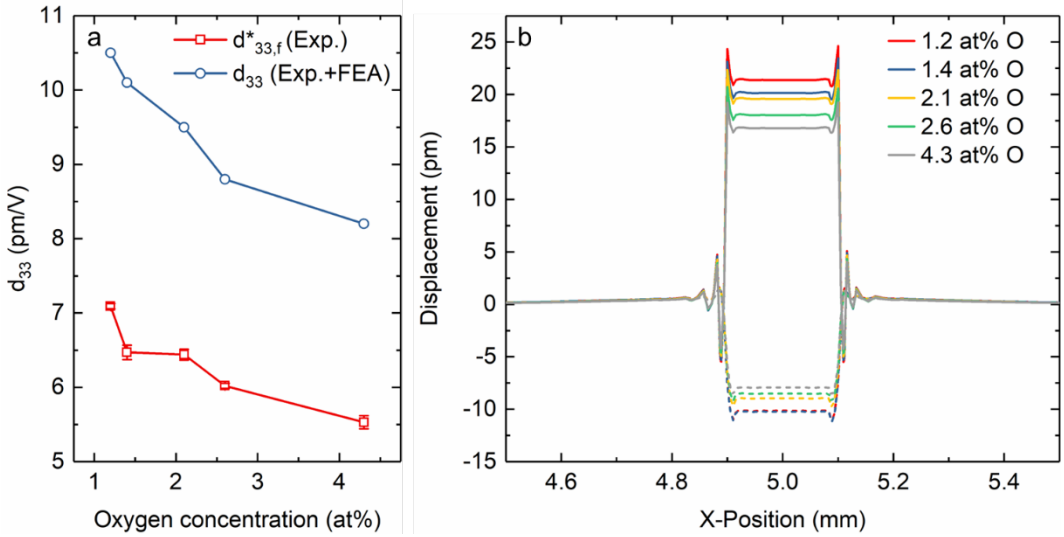

Figure 3. Piezoelectric properties of $Al_{0.65}Sc_{0.35}N$ films as a function of oxygen content. (a) Effective piezoelectric coefficient ($d^*_{33,f}$) under ac driving field at 10 kHz (square symbols), and piezoelectric coefficient (d_{33}) obtained from FEA simulation to fit the experimental data (circle symbols), (b) quantitative displacement profile of top and bottom surface of the film at active region obtained from FEA simulation.

The literature suggests that oxygen substitution at the nitrogen site (O_N) is energetically favored[22]. Since oxygen has one excess valence electron compared to nitrogen, the formation of every 3 O_N is compensated by one Al or Sc vacancy (V_{Al} or V_{Sc}). Such types of defects along with defect complexes ($3O_N$-$V_{Al\ or\ Sc}$) can create trap states in energy bandgap[23]. They

can also be charged upon trapping electrons or holes, which can affect the dielectric and piezoelectric properties of the film[43]. Alternatively, the piezoelectric response of the films is closely related to (002) FWHM[11,14,44]. Narrow FWHM is preferred for higher piezoelectric performance[45]. As we have seen in the previous section, the FWHM has increased substantially evidencing a reduction of structural coherence, which could be a reason for the observed reduction in $d^*_{33,f}$. At higher oxygen concentrations, the clustering of ($3O_N$-$V_{Al\ or\ Sc}$) defect complex can lead to the formation of various extended defects such as polarity inversion boundary or amorphous grain boundary phase[36,46]. However, no polarity inversion boundaries were observed in the TEM analysis of our samples. In previous cases of sputtered AlN and AlScN films, polarity inversion was reported when the oxygen concentration in the film exceeded 7 at% [18,19]. The oxygen concentration range investigated in this study is much lower than this value and less likely to form extended defects such as inversion boundaries. Therefore, the following sections will focus more on oxygen-related point defects.

Table I: Summary of the measured value of top surface displacement and effective piezoelectric coefficient, ($d^*_{33,f}$), piezoelectric coefficient, (d_{33}) obtained by FEA simulation to fit measured top surface displacement and DFT calculated piezoelectric coefficient (d_{33}).

Oxygen (at %)	**Experimental value**		**FEA simulation**	**DFT calculation**
	Displacement (pm)	$d^*_{33,f}$ (pm/V)	d_{33} (pm/V)	d_{33} (pm/V)
1	-	-	-	20.99
1.2	21.31 ± 0.12	7.1 ± 0.04	10.5	-
1.4	19.46 ± 0.39	6.5 ± 0.09	10.1	-
1.6	-	-	-	23.51
2.1	19.44 ± 0.19	6.4 ± 0.07	9.5	16.82
2.6	18.06 ± 0.15	6.0 ± 0.03	8.8	-
3.1	-	-	-	18.57
4.3	16.71 ± 0.24	5.5 ± 0.09	8.2	-
4.8	-	-	-	17.53

To get further insight into the trap states that may have formed due to the incorporation of oxygen, we studied the temperature dependence of conductivity and impedance spectra of $Al_{0.65}Sc_{0.35}N$ films with 4.3 at% oxygen under applied ac field of 12.5 kV/cm in the frequency range of 10^2 to 10^6 Hz. The film exhibited thermally activated DC conductivity at low frequencies (Figure 4a). The activation energy E_a estimated from the Nernst-Einstein plot (Figure 4b) is about 0.34 ± 0.017 eV. Additionally, we estimated the activation energy (E_a = 0.41 ± 0.038 eV) from the impedance relaxation (Figure 4 c-d), which is quite close to the value estimated from conductivity. Similarly, we determined activation energy for the films with

lower oxygen concentration (1.4 – 2.6 at%) as shown in Figure S8[33]. We did not find significant variation in the activation energy of the samples with different oxygen concentrations. A similar range of E_a value is reported for single crystal AlN by physical vapor transport method, which they attributed to a donor type of oxygen defect at the nitrogen site[47]. While O_N is reported to contribute to electrical conductance at moderate temperatures (27 °C- 425 °C), the charged defect complex ($3O_N$-V_{Al}) is reasoned for causing thermally activated electrical and mechanical inelastic relaxation at about 350 °C[48]. While the room temperature DC resistivity of the films ranged between 0.8 to 2.2 GΩ at 80 kV/cm, the temperature-dependent transport measurements clearly show the existence of trap states. Such trap states have been associated with leakage current, electromechanical losses, as well as dielectric relaxation in the AlN films[47,49]. For further corroboration of possible defect configuration and its effect on the piezoelectric coefficient, we modeled $Al_{1-x}Sc_xN$ with oxygen concentration in the range of 0-4.8 at% and performed first-principles calculations.

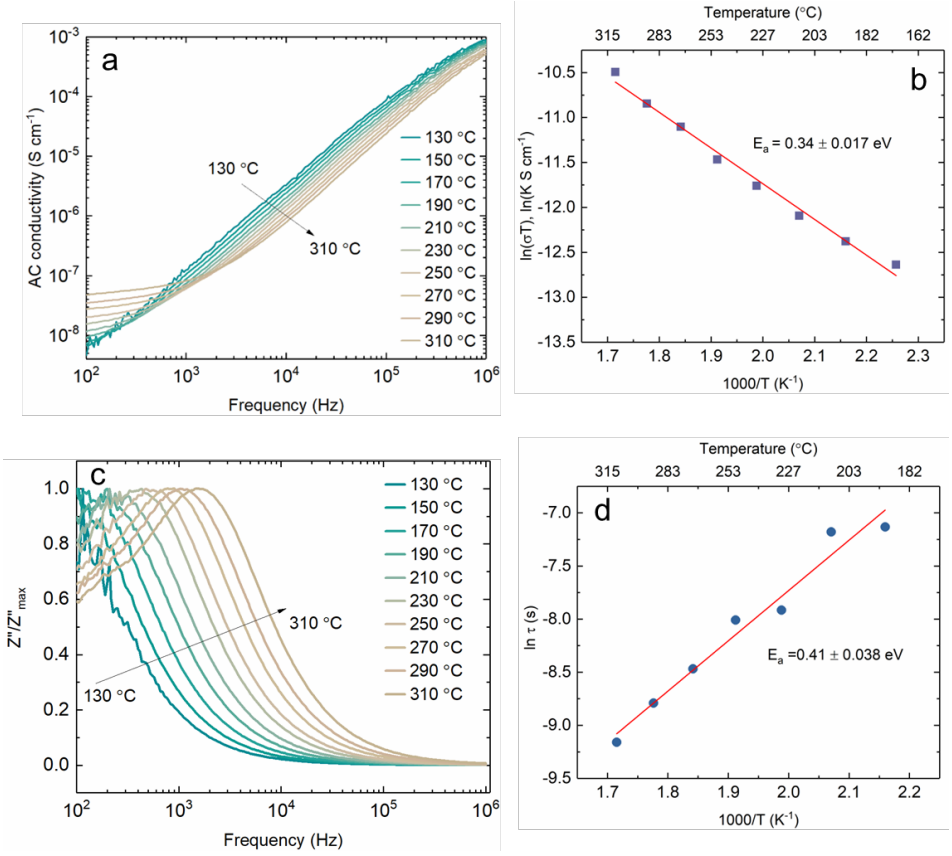

Figure 4. Electrical characterization of $Al_{0.65}Sc_{0.35}N$ films with 4.3 at% oxygen. (a) AC conductivity measured at different frequencies and temperatures. (b) Corresponding activation energy is calculated from the DC part at a lower frequency. (c) Normalized imaginary part of

complex impedance, (Z") measured at different frequencies and temperatures. (d) Activation energy is calculated from peaks from impedance relaxation at various temperatures.

B. First-principles calculations of defect formation and piezoelectric coefficients

To determine the formation energies of various oxygen and related vacancies, we constructed supercells consisting of Al, Sc, N, and O atoms with a composition close to experimental $Al_{1-x}Sc_xN$ films (i.e., with x = 0.375). In our computations, the candidate structures were constructed by the equivalent-site substitution method based on the structural symmetry as shown in Figure S5[33]. Among them, the doping configuration with the lowest total energy was selected to do the subsequent property calculations as shown in Figure S6 (see supporting information[33]). In addition, we chose models containing either 64 atoms or 96 atoms, which is large enough to avoid serious finite-size effects and small enough to keep the computational resources for further evaluation of materials parameters. The formation energy of 9 types of oxygen-related defect configurations including O_N, O_i, O_N-O_i, and $V_{Al/Sc}$-O_N (means substitution of an N atom by an O atom, an interstitial O atom, a complex of substitutional O and interstitial O, and a complex of an Al/Sc vacancy and substitutional O, respectively) with oxygen concentration in the range of 0 – 4.8% in the $Al_{0.625}Sc_{0.375}N$ supercell. For calculations, we utilized the Zhang–Northrup scheme[50], as outlined by:

$$E_f(def) = E(A_{defect}) - E(A_{perfect}) + \sum_i n_i \mu_i \quad (1)$$

Here, $E(A_{defect})$ and $E(A_{perfect})$ are the calculated total energy of the supercell with and without defects, respectively. The variables μ_i denote the chemical potential of the element added in or removed from the pristine supercell to create a defect supercell, and n_i signifies the number of atoms added in (or removed from) the pristine supercell to form the defect supercell. For the determination of the chemical potential of nitrogen μ_N in nitrogen-rich conditions, we employ Eq. (2), which is expressed as:

$$\mu_N = E_{tot}(N) - D_0(N). \quad (2)$$

The chemical potential of oxygen is computed under both oxygen-rich and oxygen-poor conditions, as expressed in Eqs. (3) and (4). In oxygen-rich conditions,

$$\mu_O = E_{tot}(O) - D_0(O). \quad (3)$$

In oxygen-poor conditions, the chemical potential of oxygen μ_O is determined by the equation:

Published in Physical Review Applied, DOI: 10.1103/PhysRevApplied.22.044071, online on 25 October 2024

$$\mu_O = \frac{1}{3}[E_{tot}(Sc_2O_3) - 2 \times \mu_{Sc}]. \quad (4)$$

Here, E_{tot}(N) and E_{tot}(O) represent the total energy of N and O atoms, respectively. The calculations are refined with the consideration of a single atom within a $25 \times 25 \times 25$ Å^3 box. D_0(N) and D_0(O) are the experimental dissociation energies of nitrogen (9.80 eV) and oxygen (5.16 eV), respectively[51]. E_{tot} (Sc_2O_3) is the total energy of Sc_2O_3 in the cubic crystal system. μ_{Sc} is the chemical potential of Sc, calculated in their metallic form. A lower formation energy at a given chemical potential means a higher equilibrium concentration of defects.

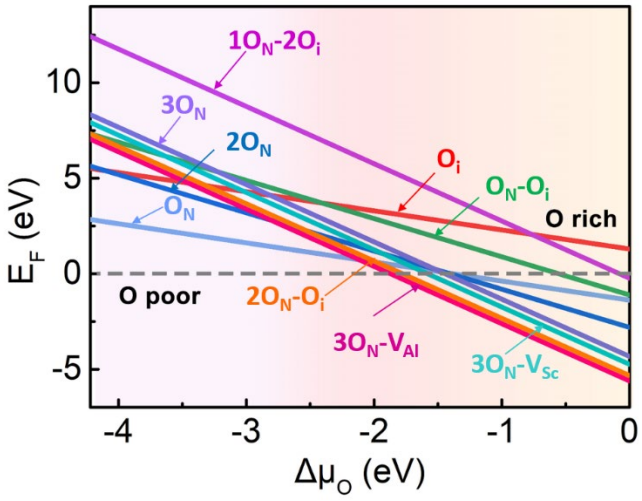

Figure 5. Defect formation energy (E_F) as a function of oxygen chemical potential for various O defect configurations in $Al_{0.625}Sc_{0.375}N$.

Figure 5 shows the results of formation energy calculations. It indicates that O_N i.e., oxygen substitution at the nitrogen site, has the lowest formation energy (2.85 eV) at low oxygen concentration conditions. Whereas interstitial oxygen (O_i) is less favorable as the formation is positive throughout the range of oxygen chemical potential. As oxygen concentration increases, the ($3O_N$-V_{Al}) complex becomes the most favourable defect (with a formation energy of -5.62 eV at high oxygen concentration). These findings conform with that previously reported and our experimental observations[22,23]. Based on the outcome of DFT calculations and activation energy of electrical conduction, we considered O_N and ($3O_N$-V_{Al}) type of defects with increasing oxygen concentrations i.e., 1% and 1.6% ($1O_N$), 2% and 3.1% ($2O_N$) and 4.8% ($3O_N$-V_{Al}) for DFT calculations of the lattice parameter and piezoelectric coefficient.

Published in Physical Review Applied, DOI: 10.1103/PhysRevApplied.22.044071, online on 25 October 2024

Theoretical piezoelectric coefficients were calculated considering contributions from both $e_{ij}^{clamped}$ and $e_{ij}^{non-clamped}$ components. The $e_{ij}^{clamped}$ represent the electronic response to the strain and $e_{ij}^{non-clamped}$ represents the local structural sensitivity to external strain. This can be expressed as follows,

$$e_{33} = e_{33}^{clamped} + e_{33}^{non-clamped} \quad (5)$$

$$where,\ e_{33}^{non-clamped} = \frac{4eZ_{33}^{*}}{\sqrt{3}\,a^2}\,\frac{du}{d\varepsilon} \quad (6)$$

Here, Z_{33}^{*} is the dynamical Born charge, *a is* the in-plane lattice parameter and *du/dε* is the sensitivity of internal parameter *u* to strain along the c-axis. The elastic coefficient C_{33} is calculated using the energy-strain method. For this purpose, a strain in the range of (-0.015 to 0.015) was applied along the c-axis and the total energy was calculated for different levels of applied strain. The computed total energy is fitted as a polynomial function of applied strain to extract the elastic coefficient C_{33}. To validate this methodology, we used w-AlN as an example. The results obtained are in good agreement with the values found in the literature. The matrix representing piezoelectric and elastic tensors ideally has three independent non-zero coefficients e_{ij} and five independent non-zero coefficients C_{ij} due to the hexagonal symmetry of wurtzite structure. However, the presence of impurities and defects reduces the symmetry of the supercell, resulting in a full set of 18 independent piezoelectric and 21 elastic coefficients (see Supporting Information[33]). Even then, the resulting matrices exhibit closer to hexagonal symmetry, as 15 of the piezoelectric coefficients and 12 of the elastic coefficients have values closer to zero.

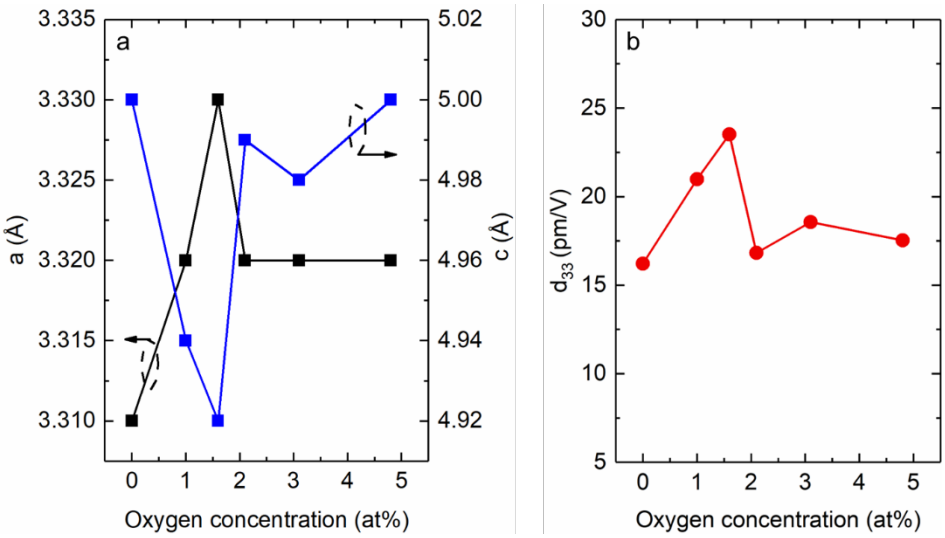

Figure 6. DFT calculations of oxygen concentration dependency on structures and piezoelectric properties. (a) Lattice parameter and (b) piezoelectric coefficient (d_{33}) of $Al_{0.625}Sc_{0.375}N$ with different oxygen concentrations and defect configurations.

Figure 6 illustrates the variation of lattice parameters and d_{33} values for $Al_{0.625}Sc_{0.375}N$ as a function of oxygen concentration obtained from DFT calculations. The lattice parameters are close to those obtained from the SAED pattern (Table SI[33]) and agree well with the literature values reported for similar composition [1]. Further, the DFT calculated d_{33} value for pristine $Al_{0.625}Sc_{0.375}N$ (i.e., without oxygen impurity) is comparable with the reported d_{33} value for similar scandium composition[52]. When a small amount (≤ 1.6%) of oxygen substitutes for the nitrogen site (O_N) without creating a vacancy, the lattice parameter *c* is found to contract while *a* expands. This is probably due to the smaller ionic size and larger electronegativity of oxygen compared to nitrogen. Interestingly, in such a case where around 1.6% of O_N is present without forming a vacancy, DFT calculations predict a 1.5-fold increase in the d_{33} value compared to the counterpart without oxygen substitutions. However, at higher oxygen concertation d_{33} decreased to lower or comparable values that of $Al_{0.625}Sc_{0.375}N$ without oxygen defects. The initial increase in d_{33} for a small amount of O_N could be due to an increase in ionicity, which is then compensated by vacancy creation that nullifies enhancement in d_{33}. Furthermore, the d_{33} values obtained by our measurement with the assistance of FEA simulations are significantly lower compared to d_{33} values obtained by DFT calculation due to the substrate clamping effect. The overall trend of measured d_{33} and that obtained from DFT calculations as a function of oxygen concentration (in the range of 1.6% - 4.8%) is consistent. It is evident from both experimental results and DFT calculations that oxygen creates various types of defects depending on its concentration in $Al_{1-x}Sc_xN$, which can potentially impact the electrical, dielectric, and piezoelectric properties of $Al_{1-x}Sc_xN$. This could be either due to the creation of localized states or local structural distortion caused by different valency, ionic size, and coordination preferences of oxygen. The localized states [shallow, O_N, or deep, ($3O_N$-V_{Al})] can induce leakage current, dielectric relaxation, and increased losses. On the other hand, local structure distortions can lead to structural incoherency, reduced crystallite size, and increased microstrain[37,46].

IV. Conclusions

In summary, we have investigated the effect of oxygen on the structural and piezoelectric properties of $Al_{0.65}Sc_{0.35}N$ thin film through both theoretical and experimental

approaches. The structural studies showed that with increasing oxygen concentration mosaicity of (002) oriented grains increased, indicating oxygen severely affects the structural coherence. The piezoelectric coefficient determined by LSV precisely with the assistance of FEA simulation showed a reduction in d_{33} value from 10.5 pm/V to 8.2 pm/V as the oxygen concentration in the film increased from 1.2 at% to 4.3 at%. Further, temperature-dependent transport studies indicated the existence of trap states with an activation energy of about 0.34 eV corresponding to the O_N point defect. DFT calculations further revealed that at lower oxygen concentrations O_N type of point defects are energetically more favorable. As oxygen concentration increases, defect complexes ($3O_N$-V_{Al}) become more favorable. DFT calculation further suggested that at low oxygen concentration (1.6 at%) where O_N type of defect is favored, the piezoelectric coefficient can be nearly 1.5 times higher compared to its counterpart without oxygen, which provide a valuable reference for future experiments. While at higher concentration, where ($3O_N$-V_{Al}) is energetically favored, the piezoelectric coefficient becomes comparable to $Al_{0.625}Sc_{0.375}N$ without oxygen. Our theoretical and experimental results show that the O_N type of oxygen point defects formed at lower concentrations may potentially enhance the piezoelectric coefficient of $Al_{0.65}Sc_{0.35}N$ thin film, while higher oxygen concentration reduces structural coherence and plays a dominant role in the degrading piezoelectric response.

Acknowledgments

The authors acknowledge support from A*STAR, under RIE2020 AME Programmatic Fund (Grant No. A20G9b0135), Singapore.

Author declarations

Conflict of interest

The authors have no conflicts to disclose.

Author Contributions

S.A. designed the experiments, data collection, and analysis, wrote the original manuscript; X.W. and L.S. conducted First-principles calculations, and data analysis; Q.X. and C.S. conducted numerical simulations; M.Z. conducted the XPS analysis; J.C. performed film growth and device fabrication; P.L. conducted the TEM analysis; L.P.C. conducted the 2D-

XRD analysis; P.Y. conducted the HRXRD at SSLS; K.Y. conceptualized and supervised the work, data analysis, review & editing of the manuscript.

Data Availability

The data that support the findings of this study are available from the corresponding authors upon reasonable request.

References

[1] M. Akiyama, T. Kamohara, K. Kano, A. Teshigahara, Y. Takeuchi, and N. Kawahara, Enhancement of piezoelectric response in scandium aluminum nitride alloy thin films prepared by dual reactive cosputtering, Adv Mater **21**, 593 (2009).

[2] S. Fichtner, N. Wolff, F. Lofink, L. Kienle, and B. Wagner, AlScN: A III-V semiconductor based ferroelectric, Journal of Applied Physics **125**, 114103 (2019).

[3] D. Jena, R. Page, J. Casamento, P. Dang, J. Singhal, Z. Zhang, J. Wright, G. Khalsa, Y. Cho, and H. G. Xing, The new nitrides: layered, ferroelectric, magnetic, metallic and superconducting nitrides to boost the GaN photonics and electronics eco-system, Japanese Journal of Applied Physics **58**, SC0801 (2019).

[4] P. Wang, D. Wang, S. Mondal, M. Hu, J. Liu, and Z. Mi, Dawn of nitride ferroelectric semiconductors: from materials to devices, Semiconductor Science and Technology **38**, 043002 (2023).

[5] L. Chen, C. Liu, M. Li, W. Song, W. Wang, Z. Wang, N. Wang, and Y. Zhu, Scandium-Doped Aluminum Nitride for Acoustic Wave Resonators, Filters, and Ferroelectric Memory Applications, ACS Applied Electronic Materials **5**, 612 (2022).

[6] C. Moe, R. H. Olsson, P. Patel, Z. Tang, M. D. Agati, M. Winters, R. Vetury, and J. Shealy, in *2020 IEEE International Ultrasonics Symposium (IUS)* (IEEE, Las Vegas, NV, USA, 2020), p. 1.

[7] N. Wang, Y. Zhu, G. L. Chua, B. Chen, S. Merugu, N. Singh, and Y. Gu, Over 10% of keff^2 Demonstrated by 2-GHz Spurious Mode-Free Sc0.12Al0.88N Laterally Coupled Alternating Thickness Mode Resonators, IEEE Electron Device Letters **40**, 957 (2019).

[8] J. X. Zheng, M. M. A. Fiagbenu, G. Esteves, P. Musavigharavi, A. Gunda, D. Jariwala, E. A. Stach, and R. H. Olsson, Ferroelectric behavior of sputter deposited $Al_{0.72}Sc_{0.28}N$ approaching 5 nm thickness, Applied Physics Letters **122**, 222901 (2023).

[9] C. Höglund, B. Alling, J. Birch, M. Beckers, P. O. Å. Persson, C. Baehtz, Z. Czigány, J. Jensen, and L. Hultman, Effects of volume mismatch and electronic structure on the decomposition of ScAlN and TiAlN solid solutions, Physical Review B **81**, 224101 (2010).

[10] M. R. Islam, N. Wolff, M. Yassine, G. Schönweger, B. Christian, H. Kohlstedt, O. Ambacher, F. Lofink, L. Kienle, and S. Fichtner, On the exceptional temperature stability of ferroelectric Al1-xScxN thin films, Applied Physics Letters **118**, 232905 (2021).

[11] M. Akiyama, K. Kano, and A. Teshigahara, Influence of growth temperature and scandium concentration on piezoelectric response of scandium aluminum nitride alloy thin films, Applied Physics Letters **95**, 162107 (2009).

[12] F. Tasnadi, B. Alling, C. Hoglund, G. Wingqvist, J. Birch, L. Hultman, and I. A. Abrikosov, Origin of the anomalous piezoelectric response in wurtzite $Sc_{(x)}Al_{(1-x)}N$ alloys, Phys Rev Lett **104**, 137601 (2010).

[13] D. F. Urban, O. Ambacher, and C. Elsässer, First-principles calculation of electroacoustic properties of wurtzite (Al,Sc)N, Physical Review B **103**, 115204 (2021).

[14] Y. Lu, M. Reusch, N. Kurz, A. Ding, T. Christoph, L. Kirste, V. Lebedev, and A. Žukauskaitė, Surface Morphology and Microstructure of Pulsed DC Magnetron Sputtered Piezoelectric AlN and AlScN Thin Films, physica status solidi (a) **215**, 1700559 (2017).

[15] S. Fichtner, N. Wolff, G. Krishnamurthy, A. Petraru, S. Bohse, F. Lofink, S. Chemnitz, H. Kohlstedt, L. Kienle, and B. Wagner, Identifying and overcoming the interface originating c-axis instability in highly Sc enhanced AlN for piezoelectric micro-electromechanical systems, Journal of Applied Physics **122**, 035301 (2017).

[16] M. D. Henry, T. R. Young, E. A. Douglas, and B. A. Griffin, Reactive sputter deposition of piezoelectric $Sc_{0.12}Al_{0.88}N$ for contour mode resonators, Journal of Vacuum Science & Technology B, Nanotechnology and Microelectronics: Materials, Processing, Measurement, and Phenomena **B 36**, 03E104 (2018).

[17] C. S. Sandu, F. Parsapour, S. Mertin, V. Pashchenko, R. Matloub, T. LaGrange, B. Heinz, and P. Muralt, Abnormal Grain Growth in AlScN Thin Films Induced by Complexion Formation at Crystallite Interfaces, physica status solidi (a) **216**, 1800569 (2018).

[18] S. K. Ryoo, K. D. Kim, H. W. Park, Y. B. Lee, S. H. Lee, I. S. Lee, S. Byun, D. Shim, J. H. Lee, H. Kim *et al.*, Investigation of Optimum Deposition Conditions of Radio Frequency Reactive Magnetron Sputtering of $Al_{0.7}Sc_{0.3}N$ Film with Thickness down to 20 nm, Advanced Electronic Materials **8**, 2200726 (2022).

[19] M. Akiyama, T. Kamohara, K. Kano, A. Teshigahara, and N. Kawahara, Influence of oxygen concentration in sputtering gas on piezoelectric response of aluminum nitride thin films, Applied Physics Letters **93**, 021903 (2008).

[20] J. Casamento, H. G. Xing, and D. Jena, Oxygen Incorporation in the Molecular Beam Epitaxy Growth of $Sc_xGa_{1-x}N$ and $Sc_xAl_{1-x}N$, physica status solidi (b) **257**, 1900612 (2020).

[21] Z. Ding, X. Cao, Q. Jia, and X. Zhang, in *Materials Science, Energy Technology & Power Engineering Iv (Mep 2021)* (AIP Conference Proceedings 2022), p. 020029.

[22] Q. Yan, A. Janotti, M. Scheffler, and C. G. Van de Walle, Origins of optical absorption and emission lines in AlN, Applied Physics Letters **105**, 111104 (2014).

[23] P. Wang, B. Wang, D. A. Laleyan, A. Pandey, Y. Wu, Y. Sun, X. Liu, Z. Deng, E. Kioupakis, and Z. Mi, Oxygen defect dominated photoluminescence emission of $Sc_xAl_{1-x}N$ grown by molecular beam epitaxy, Applied Physics Letters **118**, 032102 (2021).

[24] K. Yao and F. E. Tay, Measurement of longitudinal piezoelectric coefficient of thin films by a laser-scanning vibrometer, IEEE Trans Ultrason Ferroelectr Freq Control **50**, 113 (2003).

[25] G. Kresse and J. Furthmüller, Efficient iterative schemes for ab initio total-energy calculations using a plane-wave basis set, Physical Review B **54**, 11169 (1996).

[26] G. Kresse and J. Furthmüller, Efficiency of ab-initio total energy calculations for metals and semiconductors using a plane-wave basis set, Computational Materials Science **6**, 15 (1996).

[27] P. E. Blöchl, Projector augmented-wave method, Physical Review B **50**, 17953 (1994).

[28] J. P. Perdew, K. Burke, and M. Ernzerhof, Generalized Gradient Approximation Made Simple, Physical Review Letters **77**, 3865 (1996).

[29] J. Moellmann and S. Grimme, DFT-D3 Study of Some Molecular Crystals, The Journal of Physical Chemistry C **118**, 7615 (2014).

[30] H. J. Monkhorst and J. D. Pack, Special points for Brillouin-zone integrations, Physical Review B **13**, 5188 (1976).

[31] R. D. King-Smith and D. Vanderbilt, Theory of polarization of crystalline solids, Physical Review B **47**, 1651 (1993).

[32] R. Resta, Macroscopic polarization in crystalline dielectrics: the geometric phase approach, Reviews of Modern Physics **66**, 899 (1994).

[33] See Supporting Information at [URL will be inserted by publisher] for additional experimental results from XPS, XRD, TEM, and LSV measurements as well as details of the models used in FEA and first principles simulations.

[34] M. Moram and M. Vickers, X-ray diffraction of III-nitrides, Reports on progress in physics **72**, 036502 (2009).
[35] S. Dolabella, A. Borzi, A. Dommann, and A. Neels, Lattice Strain and Defects Analysis in Nanostructured Semiconductor Materials and Devices by High-Resolution X-Ray Diffraction: Theoretical and Practical Aspects, Small Methods **6**, e2100932 (2022).
[36] J. H. Harris, R. A. Youngman, and R. G. Teller, On the nature of the oxygen-related defect in aluminum nitride, Journal of Materials Research **5**, 1763 (1990).
[37] M. Fischer, M. Trant, K. Thorwarth, R. Crockett, J. Patscheider, and H. J. Hug, Understanding the microstructural evolution and mechanical properties of transparent Al-O-N and Al-Si-O-N films, Sci Technol Adv Mater **20**, 1031 (2019).
[38] O. Zywitzki, T. Modes, S. Barth, H. Bartzsch, and P. Frach, Effect of scandium content on structure and piezoelectric properties of AlScN films deposited by reactive pulse magnetron sputtering, Surface and Coatings Technology **309**, 417 (2017).
[39] A. Barzegar, D. Damjanovic, N. Ledermann, and P. Muralt, Piezoelectric response of thin films determined by charge integration technique: Substrate bending effects, Journal of Applied Physics **93**, 4756 (2003).
[40] P. M. Mayrhofer, E. Wistrela, M. Schneider, A. Bittner, and U. Schmid, Precise Determination of d_{33} and d_{31} from Piezoelectric Deflection Measurements and 2D FEM Simulations Applied to $Sc_xAl_{1-x}N$, Procedia Engineering **168**, 876 (2016).
[41] R. Herdier, D. Jenkins, E. Dogheche, D. Rèmiens, and M. Sulc, Laser Doppler vibrometry for evaluating the piezoelectric coefficient d33 on thin film, Review of Scientific Instruments **77**, 093905 (2006).
[42] Z. Wang, G. K. Lau, W. Zhu, and C. Chao, Influence of test capacitor features on piezoelectric and dielectric measurement of ferroelectric films, IEEE Trans Ultrason Ferroelectr Freq Control **53**, 15 (2006).
[43] Y. Feng, J. Wu, Q. Chi, W. Li, Y. Yu, and W. Fei, Defects and Aliovalent Doping Engineering in Electroceramics, Chem Rev **120**, 1710 (2020).
[44] S. Mertin, B. Heinz, O. Rattunde, G. Christmann, M.-A. Dubois, S. Nicolay, and P. Muralt, Piezoelectric and structural properties of c-axis textured aluminium scandium nitride thin films up to high scandium content, Surface and Coatings Technology **343** (2018).
[45] P. Muralt, J. Conde, A. Artieda, F. Martin, and M. Cantoni, Piezoelectric materials parameters for piezoelectric thin films in GHz applications, International Journal of Microwave and Wireless Technologies **1**, 19 (2009).
[46] P. Gasparotto, M. Fischer, D. Scopece, M. O. Liedke, M. Butterling, A. Wagner, O. Yildirim, M. Trant, D. Passerone, H. J. Hug *et al.*, Mapping the Structure of Oxygen-Doped Wurtzite Aluminum Nitride Coatings from Ab Initio Random Structure Search and Experiments, ACS Appl Mater Interfaces **13**, 5762 (2021).
[47] I. Kogut, C. Hartmann, I. Gamov, Y. Suhak, M. Schulz, S. Schröder, J. Wollweber, A. Dittmar, K. Irmscher, T. Straubinger *et al.*, Electromechanical losses in carbon- and oxygen-containing bulk AlN single crystals, Solid State Ionics **343**, 115072 (2019).
[48] J. C. Goldsby, Micro-mechanical and electrical properties of monolithic aluminum nitride at high temperatures, Journal of Alloys and Compounds **321**, 67 (2001).
[49] K. Wang and C. Wang, Aluminum‐vacancy‐related dielectric relaxations in AlN ceramics, Journal of the American Ceramic Society **101**, 2009 (2017).
[50] S. B. Zhang and J. E. Northrup, Chemical potential dependence of defect formation energies in GaAs: Application to Ga self-diffusion, Physical Review Letters **67**, 2339 (1991).
[51] K. P. Huber and G. Herzberg, *Molecular Spectra and Molecular Structure* 1979).
[52] A. A. M. Noor, O. Z. Olszewski, H. Campanella, and M. Nolan, Large Piezoelectric Response and Ferroelectricity in Li and V/Nb/Ta Co-Doped w-AlN, ACS Appl Mater Interfaces **13**, 944 (2021).

Published in Physical Review Applied, DOI: 10.1103/PhysRevApplied.22.044071, online on 25 October 2024